International Journal of Pharmaceutics 640 (2023) 123015

Contents lists available at ScienceDirect

International Journal of Pharmaceutics

journal homepage: www.elsevier.com/locate/ijpharm

# Polysaccharide-protein microparticles based-scaffolds to recover soft tissue loss in mild periodontitis

Marco Ruggeri [a], Martina Lenzuni [b], Giulia Suarato [b], Barbara Vigani [a], Cinzia Boselli [a], Antonia Icaro Cornaglia [c], Daniele Colombo [a], Pietro Grisoli [a], Caterina Ricci [d], Elena Del Favero [d], Silvia Rossi [a], Athanassia Athanassiou [b], Giuseppina Sandri [a,*]

[a] Department of Drug Sciences, University of Pavia, Viale Taramelli 12, 27100 Pavia, Italy
[b] Smart Materials, Istituto Italiano di Tecnologia, Via Morego 30, 16163 Genova, Italy
[c] Department of Public Health, Experimental and Forensic Medicine, University of Pavia, via Forlanini 2, 27100 Pavia, Italy
[d] Department of Medical Biotechnology and Translational Medicine, University of Milan, LITA Viale Fratelli Cervi 93, 20090 Segrate, Italy

ARTICLE INFO

*Keywords:*
Mild periodontitis
Gums
Silk fibroin
Mucoadhesive properties
*In vivo* wound model

ABSTRACT

Periodontal regeneration is extremely limited and unpredictable due to structural complications, as it requires the simultaneous restoration of different tissues, including cementum, gingiva, bone, and periodontal ligament. In this work, spray-dried microparticles based on green materials (polysaccharides – gums - and a protein - silk fibroin) are proposed to be implanted in the periodontal pocket as 3D scaffolds during non-surgical treatments, to prevent the progression of periodontal disease and to promote the healing in mild periodontitis. Arabic or xanthan gum have been associated to silk fibroin, extracted from Bombyx mori cocoons, and loaded with lysozyme due to its antibacterial properties. The microparticles were prepared by spray-drying and cross-linked by water vapor annealing, inducing the amorphous to semi-crystalline transition of the protein component. The microparticles were characterized in terms of their chemico–physical features (SEM, size distribution, structural characterization – FTIR and SAXS, hydration and degradation properties) and preclinical properties (lysozyme release, antibacterial properties, mucoadhesion, *in vitro* cells adhesion and proliferation and in vivo safety on a murine incisional wound model). The encouraging preclinical results highlighted that these three-dimensional (3D) microparticles could provide a biocompatible platform able to prevent periodontitis progression and to promote the healing of soft tissues in mild periodontitis.

## 1. Introduction

Periodontitis is a chronic disease affecting the tissues surrounding the teeth and is predominantly caused by bacterial infections that attack the protective and supportive tissues of the tooth (Budai-Szűcs et al., 2021). Fundamentally, periodontal disease is initially triggered by bacteria or bacterial metabolic products leading to inflammatory responses and the subsequent destruction of the periodontal tissues and the interconnected tooth-supporting structures (Könönen et al., 2019). Recent clinical microbiome investigations in preclinical models proved that periodontitis is a dysbiotic disease, characterized by a a multistep process in which the proportion of existing microbial species changes as new colonizers emerge (Zhang et al., 2020; Abusleme et al., 2021). Griffen and co-workers reported that 123 bacterial species were detected in patients deep pockets with periodontitis, while 53 species were found in healthy tissues (Griffen et al., 2012). Reduction of lysozyme concentration in the oral cavity enhances the growth of conditionally pathogenic or pathogenic microorganisms (Dekina et al., 2016) and the occurrence of periodontitis (Ito et al., 2008). The current classification identifies three types of periodontitis: (a) necrotizing periodontitis, (b) periodontitis as a manifestation of systemic disease and (c) periodontitis (which include subtypes of “chronic” and “aggressive” ones) (Graetz et al., 2019). These are classified based on a multi-dimensional staging and grading system (Abrahamian et al., 2022). Staging is related on the severity of disease, on the extent of destroyed and damaged tissue, and on the complexity of disease management, while grading furnishes supplementary information on biological features of the disease such as the evidence of progression, the bone loss/age, the type of biofilm deposits and the risk of factors (mainly smoking and diabetes) (Tonetti et al., 2018). Common features include bone resorption (both vertically

* Corresponding author at: Department of Drug Sciences, University of Pavia, Viale Taramelli 12, 27100 Pavia, Italy.
*E-mail address:* g.sandri@unipv.it (G. Sandri).

https://doi.org/10.1016/j.ijpharm.2023.123015
Received 22 December 2022; Received in revised form 28 April 2023; Accepted 29 April 2023
Available online 6 May 2023
0378-5173/© 2023 The Author(s). Published by Elsevier B.V. This is an open access article under the CC BY-NC-ND license (http://creativecommons.org/licenses/by-nc-nd/4.0/).

along apex and horizontally) and loss of the epithelial attachment over 6 mm, with consequent tooth loss. In addition to progressive loss of periodontal tissue, it has been reported that periodontal disease is a cofactor of systemic diseases, such as diabetes mellitus, and cardiovascular, liver, or pulmonary diseases (Albandar et al., 2018; Carrizales-Sepúlveda et al., 2018; Reynolds and Duane, 2018).

Therapeutic approaches aim to eliminate inflammation, to prevent the disease progression, and to recover the tissue loss. They consist of mechanical removal of bacterial deposits and calculus from the subgingival environment using non-surgical or surgical treatments. Both the treatments produce significant clinical results, although severe disease (deeper pockets) tends to benefit better from surgical therapy. However, the incidence of disease progression is directly related to pocket depth, since the deeper the pocket, the fewer subgingival bacterial deposits are removed, and these induce reoccurrence. Despite many concerns about antibiotic resistance, the antibacterial chemotherapeutics and antibiotics provide additional benefits in chronic periodontitis treatments (Shaddox and Walker, 2010).

Although many studies in periodontal tissue engineering have been tremendously promising for novel therapeutic developments, many challenges remain inconclusive (Kim et al., 2014; Park, 2019). In fact, periodontal tissue regeneration is extremely limited and unpredictable due to structural complications, considering the presence of hierarchical constructs with micron-scaled dimensions, and requires tissue integrations for a complete function restoration. Different strategies in the regenerative medicine have been recently proposed to attempt regeneration of periodontal tissues and to promote tooth-supporting function restorations (Park et al., 2017). In this context, gums-based biomaterials can be considered as potent candidates to enhance the healing of soft periodontal tissues and its function. These biomaterials show biocompatibility, low immunogenicity, acceptable biodegradation rate, and structure similar to the natural extracellular matrix (ECM) (Bilal et al., 2022). In this work, two different gums have been considered: arabic gum (GA) and xanthan gum (GX). GA is composed of 2–6 units of 1,3-linked β-D-galactopyranosyl conjugated to a backbone of 1,3-linked β-D-galactopyranosyl by 1,6-linkages. Its biologic effect includes the enhancement of dental tissue remineralization due to its rich content of calcium, magnesium, and potassium salts, and the suppression of acid dependent demineralization, thus contributing to the remineralization (Grohe and Mittler, 2021). This has been proved in a murine model (Onishi et al., 2008). GX is an anionic exocellular polysaccharide, extracted from the bacterium *Xanthomonas campestris*, and it is composed of a linear chain of D-glucose linked in 1,4-positions to-D-mannose-(1,4)-D-glucuronic acid-(1,2)-R-D-mannose attachments. GX and GX-based biomaterials have extensively been used in a wide range of applications from foods and food-packaging to cosmetics and drug delivery due to its rheological properties of forming highly viscous solution at low shear forces, and high pseudo-plasticity (Kumar et al., 2018). Moreover, it is well known for its non-toxicity and excellent biocompatibility.

Given these premises, the aim of this work was the design and the development of spray-dried microparticles based on polysaccharides - gums- and a protein - silk fibroin, as 3D scaffolds, to be implanted in the periodontal pocket especially during non-surgical treatments, to prevent the progression of periodontal disease and to promote the healing of soft tissue in mild periodontitis. GA or GX have been associated to silk fibroin (SF), a structural protein of the *Bombyx mori* cocoons, widely studied in the past decade for biomedical applications, such as skin care, wound healing tissue regeneration and drug delivery (Pritchard et al., 2013; Sheng et al., 2013; Yang et al., 2013; Zhang et al., 2016). Gums and fibroin have been selected since they are green and safe materials due to their bio-derivation and water solubility (Scalia et al., 2021). In addition, lysozyme (LZ), a compact globular protein made of 129 amino acid residues naturally present in saliva, and mucus, has been chosen to be loaded into the microparticles due to its antibacterial properties (Wu et al., 2017; Xiao et al., 2021). Although there is evidence in literature of gums, fibroin and their blends-based systems (mainly hydrogels, but also microparticles and spun fibers), the novelty of the microparticles here described is related to their solubility. In fact, microparticles were prepared by spray-drying (SD) and cross-linked by water vapor annealing to obtain insoluble scaffolds starting from aqueous polymeric blends, without the use of chemicals and potentially toxic cross-linkers. Moreover, the one step manufacturing process here proposed is easy scalable, to allow a fast translation to clinics in order to improve cells proliferation and tissue regeneration. Furthermore, the microparticles were characterized using a multidisciplinary approach: chemico–physical properties (SEM, size distribution, structural characterization - FTIR, SAXS –and hydration properties), and preclinical properties (lysozyme release, mucoadhesion, *in vitro* cells adhesion and proliferation and in vivo safety on a murine incisional wound model) were assessed.

## 2. Materials and methods

### 2.1. Materials

Arabic gum (Mw 3.8 × $10^5$ Da, Agri-Rapid Acacia® RE, Agrigum, Roquette, Giusto Faravelli, Milan, Italy); xanthan gum from Xanthomonas campestris (Mw 2.2 × $10^6$ Da, Sigma-Aldrich, Milan, Italy); lysozyme (LZ) from chicken egg white (Mucopeptide N-acetylmuramoylhydrolase, Muramidase, crystalline powder, ~70000 UI/mg Sigma-Aldrich, Milan, Italy) were used for microspheres preparation.

### 2.2. Methods

#### 2.2.1. Silk fibroin regeneration

Fibroin was extracted from *Bombyx mori* cocoons, according to Pignatelli et al. (2018). The cocoons were cut in small pieces (up to 5 gr) and boiled for 30 min in an aqueous solution (2 l) of $Na_2CO_3$ (0.023 M), to allow for the degumming of the silk. Afterwards, the obtained yarn was washed three times in MilliQ water and let dry under a fume hood overnight. Degummed fibroin fibers were solubilized in 9.3 M lithium bromide at 60 °C for 5 h and subsequently dialyzed by means of dialysis tubes (MW cut off 3500 Da, Spectrum Labs) against MilliQ water for 3 days, changing the dialysis water twice a day. The dialyzed samples were centrifuged twice at 9000 rpm and 4 °C (15 min per run) and stored in the refrigerator. To quantify the extracted protein concentration, 1 ml of dialyzed fibroin solutions was left to dry overnight under a fume hood, at room temperature. The concentration was obtained by weighing the dried film deposited due to water evaporation. Values were found to be in the range of 50–60 mg/ml for each batch produced.

#### 2.2.2. Preparation of spray-dried microparticles

Fig. 1a reports the quali-quantitative compositions of the polymeric blends. Briefly, two different polymeric blends were prepared by mixing GA or GX with SF in aqueous solution.

Microparticles were prepared by spray-drying (SD) using a Buchi 190 mini spray drier (Büchi Labortechnik AG, Germany) with 0.5 mm nozzle. The polymeric blends were fed to the nozzle via peristaltic pump (spray flow rate of 16 ml/min.). The solutions were sprayed as atomized droplets by the force of the compressed air (air flow rate of 4 lb per square inch) and the solvents in the droplets were evaporated in a drying chamber by hot air (inlet air temperature of 200 °C and outlet air temperature of 140 °C). The dried products were collected in a collection vessel and weighed. The process yield was always higher than 50%. Microparticles were then cross-linked by water vapor annealing (WVA) for 6 h at 50 °C, in the following paragraphs defined as (c), while the non-crosslinked samples will be labelled as (nc).

Analogously, LZ loaded microparticles were prepared by adding lysozyme to each polymer blend and manufactured as previously described.

a)

| % w/w | Arabic gum (GA) | Xanthan gum (GX) | Fibroin (SF) | Lysozyme (LZ) |
|---|---|---|---|---|
| GA | 0.25 | -- | 0.15 | -- |
| GA-LZ | 0.25 | -- | 0.15 | 0.05 |
| GX | -- | 0.25 | 0.15 | -- |
| GX-LZ | -- | 0.25 | 0.15 | 0.05 |

b)

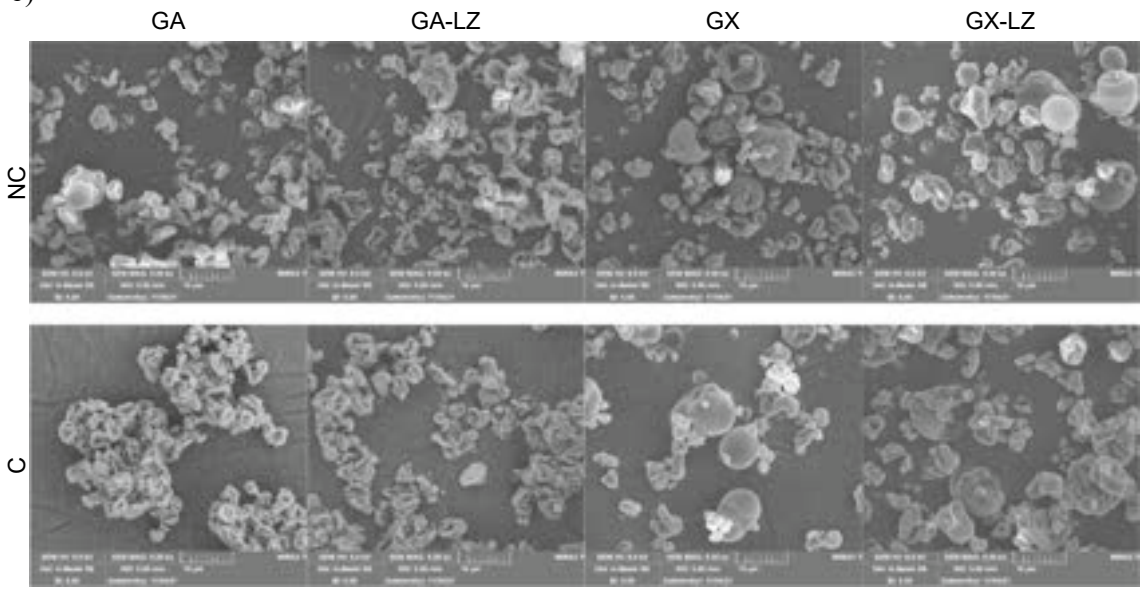


c)

| Sample | | d10 (μm) | d50 (μm) | d90 (μm) | d[4,3] (μm) | SPAN |
|---|---|---|---|---|---|---|
| GA | nc | 2.64±0.58 | 5.52±0.84 | 16.05±2.38 | 9.51±1.54 | 2.44±0.19 |
| | c | 4.77±0.05 | 10.82±0.48 | 23.19±1.76 | 12.58±0.69 | 1.70±0.11 |
| GA-LZ | nc | 3.38±0.03 | 6.76±0.07 | 15.12±0.56 | 8.27±0.20 | 1.74±0.08 |
| | c | 5.07±0.09 | 9.81±0.32 | 18.69±1.02 | 10.95±0.44 | 1.39±0.06 |
| GX | nc | 3.93±0.07 | 12.76±0.72 | 35.85±1.37 | 16.69±0.57 | 2.51±0.12 |
| | c | 6.99±0.73 | 14.67±2.26 | 30.16±6.01 | 16.83±2.77 | 1.57±0.24 |
| GX-LZ | nc | 3.97±0.07 | 10.19±0.82 | 31.80±6.94 | 14.70±2.55 | 2.70±0.46 |
| | c | 5.58±0.78 | 11.35±2.20 | 24.07±7.94 | 13.28±3.38 | 1.58±0.32 |

**Fig. 1.** a) Composition (% w/w) of polymeric blends used to prepare the microparticles, b) SEM micrographs of spray-dried microparticles – scale bar 10 μm, c) statistical particle diameter: d10, d50, d90, d[4:3] and SPAN factor (mean ± s.d.; n = 3) of microparticles before (nc) and after crosslinking (c).

*2.2.3. Microparticles characterizations*

The microparticles morphology was assessed by SEM (Tescan, Mira3XMU, Brno, Czech Republish, CISRIC, University of Pavia). Samples were mounted on metal stubs using a double-sided adhesive tape and sputtered by means of carbon deposition under vacuum. The morphology of the microparticles were analyzed before and after crosslinking.

Particle size distribution was determined using a Malvern Mastersizer 3000E granulometer (Malvern Instruments™). Microsphere suspensions were prepared in isopropanol to avoid possible swelling and solubilization. Particle diameters (d10, d50, d90) were calculated together with the SPAN factor as an index of the amplitude of particle size distribution.

Infrared spectra were measured by means of Fourier Transform Infrared (FTIR) spectrometer (Equinox 70 FT-IR, Bruker, MA, USA). Approximately 4 mg of each sample were mixed with 150 mg of potassium bromide (KBr) and pressurized to achieve a transparent pellet. All the spectra were acquired in the spectral range 4000 – 600 $cm^{-1}$, with a scanning resolution of 4 $cm^{-1}$, accumulating 128 scans. Deconvolution of the silk fibroin Amide I peak was performed as previously reported by Guzman-Puyol et al. (2016). The wavenumber positions of the different peak components were derived via calculation of the second-order derivative. The fitting of the various contributions was performed using Gaussian-shaped peaks, keeping as boundary conditions the following: peak area greater than zero, full width at half maximum between 5 and 15. The different contributions to the overall protein molecule conformation were therefore calculated from the ratio between the areas pertaining to the specific peaks and the total area of the Amide I peak (used as reference).

Small Angle X-ray Scattering experiments were carried out at the ID02 SAXS beamline of ESRF (Grenoble, France). Dry microparticles were put in Kapton capillaries and fully hydrated with water. The scattered intensity was acquired on a 2D detector at two different sample-to-detector distances, namely 1 m and 10 m. After angular regrouping and background subtraction, the joined spectra report the scattered intensity as a function of the momentum transfer q in the region 0.006 $nm^{-1} < q < 6\ nm^{-1}$ where $q = 4\pi\sin(\theta/2)/\lambda$, being θ the scattering angle and λ = 0.1 nm the radiation wavelength.

*2.2.4. In vitro hydration and degradation*

The increase of microparticle diameters upon hydration was analyzed *in vitro* to evaluate the SD microparticles swelling.

Microparticle suspensions were prepared in simulated artificial saliva (SAS: NaCl 0.125 g/l; KCl 0.964 g/l, KSNC 0.189 g/l, $KH_2PO_4$ 0.655 g/l, urea 0.2 g/l, $CaCl_2 2H_2O$ 0.229 g/l, $Na_2SO_4 10H_2O$ 0.763, $NH_4Cl$ 0.178, $NaHCO_3$ 0.631, pH 6.7) and gently stirred for 24 or 48 h (Pietrzyńska and Voelkel, 2017). Then the particle diameters were measured using DLS as previously described (paragraph 2.2.3). Swelling Index (SI) (Gavini et al., 2008) was calculated as follows:

$$SI = \frac{d[4:3]_t - d[4:3]_0}{d[4:3]_0}$$

Where d[4:3]t is the volume weighted mean diameter at t time and d [4:3]0 is the volume weighted mean diameter at time 0.

The *in vitro* degradation was performed by incubating the microparticles in SAS at 37 °C. After 24 and 48 h, microparticles were collected and the weight residues (%) were calculated.

After 48 h, the SD microparticle morphology was evaluated using SEM, as previously described (paragraph 2.2.3.).

### 2.2.5. Lysozyme release

Fifty mg of microparticles were placed in 10 ml of SAS at 37 °C to simulate microparticles implant in the periodontal pocket. At prefixed times, the supernatants were collected, and assayed to quantify the lysozyme release by means of a Lysozyme Detection Kit (Sigma-Aldrich, Milan, Italy). In a 96-well plate, 200 µl of *Micrococcus lysodeikticus* suspension were put in each well and, when the absorbance reached the constant value, 7.5 µl of supernatants were added. After 5 min of incubation, the absorbance was detected using FLUOstar® Omega Microplate Reader and the units/ml were calculated as follows:

$$\frac{Units}{ml} = \frac{(\Delta A_{450} test - \Delta A_{450} test)(df)}{(0.001)(0.0075)}$$

Where df is the dilution factor, 0.001 the Absorbance at 450 nm as per the Unit Definition and 0.0075 the volume (ml) of enzyme solution.

### 2.2.6. Antimicrobial properties

The antimicrobial properties of the microparticles were assessed against *Streptococcus mutans* ATCC 25175. Before testing, bacteria were cultured in Brain Hearth Infusion Broth (BHB, Oxoid, Basingstoke, UK) at 37 °C. The cultures were centrifuged at 224 g for 20 min to separate microorganisms from culture broth and then washed with purified water. Washed cells were re-suspended in Dulbecco's PBS and optical density (OD) was adjusted to 0.2, corresponding approximately to $10^7$-$10^8$ colony forming units (CFU)/ml at 650 nm wavelength. The antibacterial activity was determined with the macrodilution broth method, according to Clinical and Laboratory Standards Institute guidelines (2009). The minimum inhibitory concentration (MIC) was evaluated after 24 h incubation at 37 °C as the lowest concentration that completely inhibited the formation of visible microbial growth. The MBC was the lowest concentration resulting in greater than 99.9% reduction of the initial inoculum after 24 h incubation at 37 °C. Aliquots were inoculated with 1 day release samples, and stock standard solutions of ampicillin were used as a positive control. Control test tubes containing microorganisms in culture without lysozyme were used.

### 2.2.7. Mucoadhesion measurements

Mucoadhesive properties of GA, GA-LZ, GX and GX-LZ were investigated by means of a texture analyser TA.XT plus Texture Analyzer (Stable Micro Systems, Godalming, UK) equipped with a 5 kg load cell and P/10 measuring system, consisting of a cylindrical probe with a diameter of 10 mm (Ø=10 mm) and A/MUC measuring system. Disks (1 cm diameter) were obtained by compressing 50 mg microparticles at 2 t for 10 s (thickness 0.7 mm) and were fixed onto the sample holder using bi-adhesive tape. Thirty µl of a 4% w/w mucin solution (type I from bovine submaxillary glands, Sigma-Aldrich, Italy) in SAS were layered on a filter paper disc (Ø: 10 mm) fixed to the cylindrical probe. The probe was lowered and the microparticle disk was put in contact with the mucin dispersion. A preload of 2500 mN was applied for 60 s, then the probe was withdrawn at a constant speed (2.5 mm/s) up to the complete separation of the mucin-disk interface. Blank measurements were performed using 30 µl SAS instead of mucin dispersion. The maximum detachment force (Fmax, mN) and work of adhesion (AUC, mN.mm) were measured (Sandri et al., 2004).

### 2.2.8. Cells adhesion and proliferation

Adhesion and proliferation assay was carried out using normal human dermal fibroblasts (NHDF) from juvenile foreskin (PromoCell, VWR, Milan, Italy) and hASCs cells (ZenBio (Durham, NC, USA). Fibroblasts were grown in the presence of Dulbecco's modified Eagle medium (DMEM, Sigma-Aldrich, Milan, Italy) supplemented with 10% v/v fetal bovine serum (Euroclone, Milan, Italy), and with penicillin/streptomycin solution (pen/strep, 100 UI/100 µg/ml, Sigma-Aldrich, Merck, Milan, Italy), while hASCs were grown in basal-α-MEM medium based on 1% of minimum essential medium (MEM, ZenBio, Durham, NS, USA), supplemented with 10% FBS (fetal bovine serum, Euroclone, Milan, Italy), 0.22% bicarbonate, and with penicillin/streptomycin solution (pen/strep, 100 UI/100 µg/mL, Sigma-Aldrich, Merck, Milan, Italy) at 37 °C in a 5% $CO_2$ atmosphere. Fifty mg of microparticles disks (prepared as previously described in paragraph 2.2.5) were placed in a 24-well plate well bottom (flat bottom, Cellstar©, Greiner bio-one, Frickenhausen, Germany) and fibroblasts or hASCs were seeded onto the disk at a seeding density of 35,000 cells/well and grown for 3 or 6 days. After 3 or 6 days, the AlamarBlue (Thermo Fisher Scientific, Italy) assay was performed. The growth medium was removed from the wells and 400 µl of an AlamarBlue solution (10% w/w in DMEM w/o phenol red) were placed and incubated at 37 °C for 3 h. Finally, the AlamarBlue was transferred in a 96-well plate and the fluorescence was detected using FLUOstar® Omega Microplate Reader using 560 nm as λex and 590 nm as λem (Ruggeri et al., 2022a). After three washing, the cells grown onto the microparticles disks were subjected to the staining of cell actin cytoskeleton with phalloidin FITC Atto 488 (50 µl at 20 µg/ml in PBS in each well, contact time 30 min, Sigma-Aldrich, Milan, Italy) and of the cell nuclei with Hoechst 33,258 (100 µl of solution at 1:10,000 dilution in PBS per each well, contact time 10 min, Sigma-Aldrich, Milan, Italy). Finally, the samples were mounted onto glass slides, covered with coverslips and analyzed using CLSM (Leica TCS SP2, Leica Microsystems, Milan, Italy) at λex = 346 nm and λem = 460 nm for Hoechst 33258, and λex = 501 nm and λem = 523 nm for phalloidin FITC.

### 2.2.9. Preliminary preclinical evaluation on in vivo model

All animal experiments were carried out in full compliance with the standard international ethical guidelines (All animal experiments were carried out in full compliance with the standard international ethical guidelines (EU Directive 2010/63/EU) approved by Italian Health Ministry (D.L. 116/92). The study protocol was approved by the Local Institutional Ethics Committee of the University of Pavia for the use of animals and by ISS (Istituto Superiore di Sanità). Six male rats (Wistar 200–250 g, Envigo RMS S.r.L.) were anesthetized with equitensine at 3 ml/kg (39 mM pentobarbital, 256 mM chloral hydrate, 86 mM $MgSO_4$, 10% v/v ethanol, and 39.6% v/v propylene glycol) and shaved to remove all hair from their backs. All animals were then carefully monitored for the following 3 days by animal care services and received additional treatment of the same pharmacological treatments. To evaluate the system safety, 50 mg of microparticles were subcutaneously implanted in an 8 mm incision in the rat back. The incisions were then sutured using strips (Steri-Strip Suture, I). Eighteen days after the treatment, the rats were sacrificed, and full thickness biopsies were taken in correspondence to the incisions and the histological analysis was performed.

A biopsy of intact skin was also taken for comparison and the lesions treated with 20 µl saline solution were the negative control. Tissue samples were bisected along the wildest line of the wound, immediately

immersed in the fixative solution (10% neutral buffered formalin), embedded in paraffin, and sectioned at a thickness of 5 μm. Some sections were stained with hematoxylin and eosin (H&E), others with picrosirius red (PSR).

Picrosirius red stain was applied as follows: deparaffinized sections were hydrated, faintly stained with Weigert's hematoxylin for nuclei, and stained with PSR (1 h). Then all sections were dehydrated, cleared in xylene, and mounted with DPX. Stained sections were observed with a light microscope Carl Zeiss Axiophot provided, for circular polarizing microscopy, with suitable filters in the condenser stage and in the microscope tube. Images were recorded through a microscope digital 5 megapixels CCD camera Nikon DS - Fi2.

#### 2.2.10. Statistical analysis

Statistical analyses were performed using Astatsa statistical calculator. One-way analysis of variance (ANOVA) was followed by Scheffè for *post-hoc* comparisons. A value $p < 0.05$ was considered significant.

## 3. Results and discussion

### 3.1. Microparticles characterization

Fig. 1b shows the SEM micrographs of SD microparticles (left column – before cross-linking, right column – after cross-linking). Different morphologies are observed for the GA and GX SD microparticles. In particular, GA microparticles are heterogeneous and characterized by concavities and roughness with porous fractured surfaces. The GX SD microparticles have a spherical shape although some cavities are evident at the surface. The different morphologies could be related to the molecular weight and the concentration of the polymers and consequently to the viscosity of the polymeric blends. It can be supposed that GX, having a molecular weight higher than that of GA, could act as a plasticizer due to its pseudoplastic properties leading to the formation of spherical and smooth surface microparticle.

On the other hand, independently of the polysaccharide type, the presence of LZ does not alter the microparticles morphology. Water vapor annealing was selected as the crosslinking process, being able to induce SF transition from soluble to insoluble conformation. In fact, SF is a fibrous protein with a semi-crystalline structure and its conformation depends on its relative content of secondary structures. The SF main

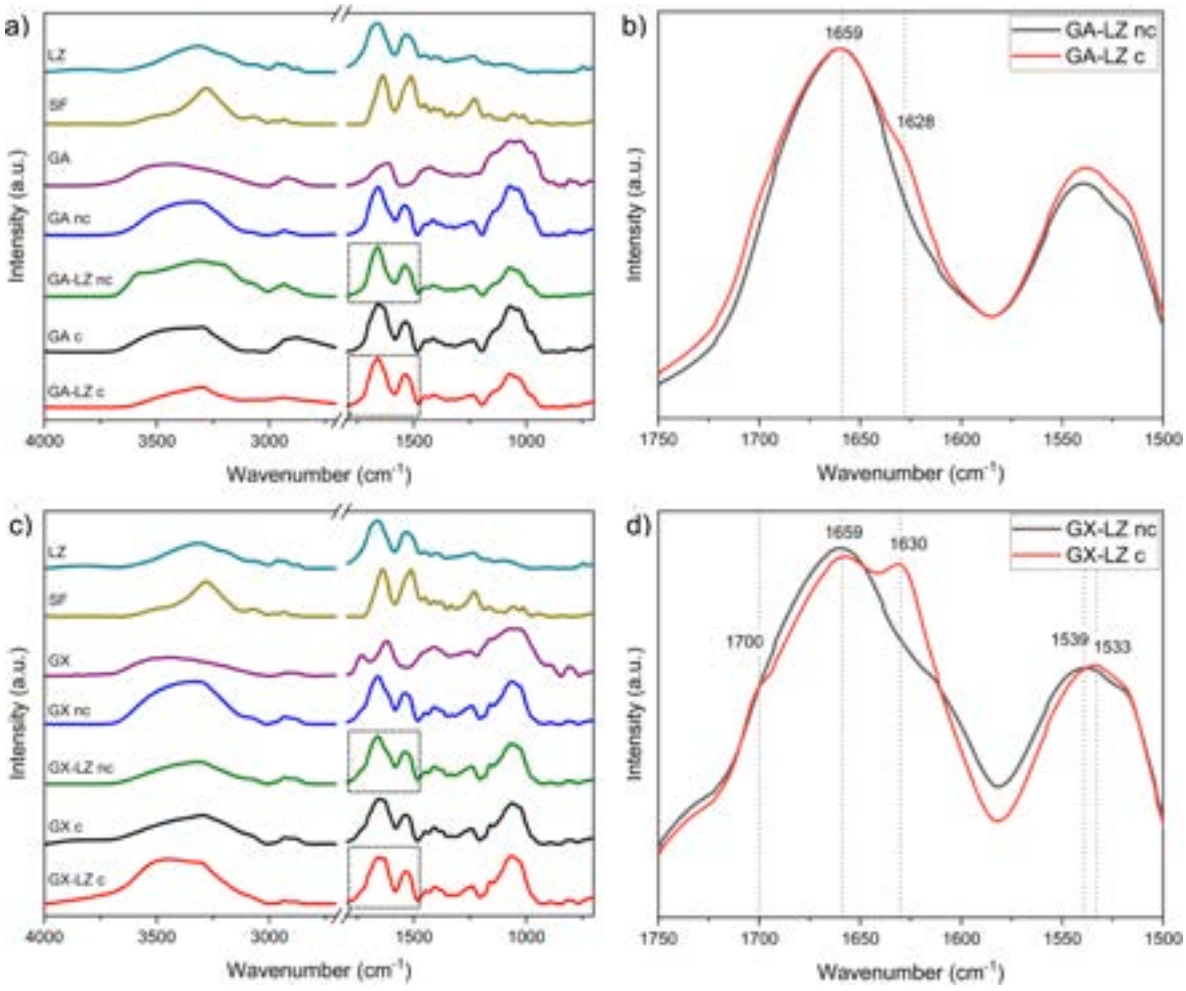


**Fig. 2.** a) FTIR spectra of all the pristine components used for the arabic gum microparticles preparation (SF, GA– both cross-linked (c) and non-cross-linked (nc), lLZ), stacked for comparison with the spectra of the GA and composite GA-LZ microparticles before and after the cross-linking treatment. b) zoomed FTIR spectra of the GA-LZ microparticles, either c or nc, in the amide I and amide II regions. c) FTIRspectra of all the pristine components used for the xanthan gum microparticles preparation (SF, GX – both crosslinked (c) and non-crosslinked (nc), LZ), stacked for comparison with the spectra of the composite GA-LZ microparticles before and after the cross-linking treatment. d) zoomed FTIR spectra of the GX-LZ microparticles, either c or nc, in the amide I and amide II regions. and GX and GX-LZ microparticles after and before cross-linking. SAXS spectra of GA nc and GA c (e), GX nc and GX c (f) microparticles, together with their pristine components (silk fibroin, arabic gum, xanthan gum); SAXS spectra of GA and GA-LZ (g), GX and GX-LZ (h).

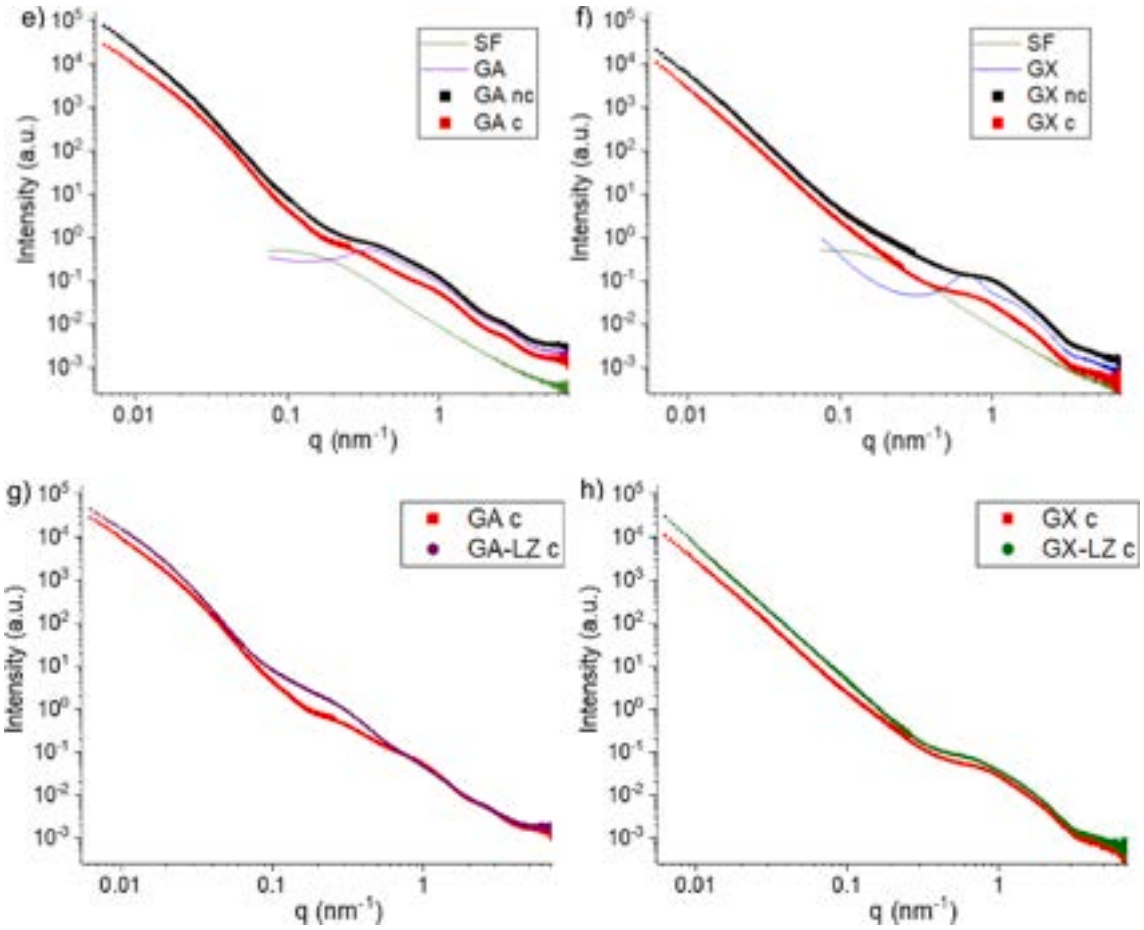


**Fig. 2.** (*continued*).

conformations are silk I and silk II. Silk I is a metastable structure with a zigzag amorphous conformation, characterized by a dominant number of random coils and α-helix, resulting in instable and water-soluble macromolecules (Johari et al., 2020). On the other hand, silk II presents highly ordered β-sheet regions, which are responsible for an increased crystallinity, leading to its stability, water-insolubility, and thermal and mechanical resistance (Dubey et al., 2015; Qi et al., 2017). In particular, the water vapor annealing treatment of the SD microparticles induced the transition from the amorphous state silk I to the crystalline silk II (Pignatelli et al., 2018), allowing to obtain insoluble substrates in aqueous environment without losing of structural integrity and morphology of the samples, and avoiding the use of potentially cytotoxic solvents. Moreover, the cross-linking process does not affect the microparticles morphology.

Fig. 1c reports the microparticle diameters and SPAN factor (width of the size distribution) before (nc) and after crosslinking (c). All the SD microparticles show a narrow particle size distribution with a mean diameter d[4:3] between 8 and 17 μm. No significant differences in presence of lysozyme were observed for both gums-based systems. GA-based microparticles are smaller than those based on GX: GX produces highly pseudo-plastic dispersions due to its rigid network leading to the formation of larger droplets and, hence, microparticles with a greater diameter (Dabestani and Yeganehzad, 2019).

Fig. 2 reports the FTIR profiles of the microparticles before and after cross-linking treatments, as well as the spectra of their pristine components (i.e. silk fibroin, Arabic gum, Xanthan gum, and lysozyme). The FTIR spectra of SF and LZ show the typical protein fingerprints, including the Amide I (1638 cm$^{-1}$ and 1661 cm$^{-1}$), Amide II (1512 cm$^{-1}$ and 1535 cm$^{-1}$) and Amide III (1231–1167 cm$^{-1}$ and 1234–1173 cm$^{-1}$) peaks. GA and GX are complex mixtures of carbohydrates which contain many different types of O–H and C-O bonds, and, hence, present more convoluted O–H stretching and C-O stretching regions from 3600 cm$^{-1}$ to 3300 cm$^{-1}$ and from 1200 cm$^{-1}$ to 800 cm$^{-1}$, respectively (Faria et al., 2011; Sowunmi et al., 2020).

The spectra of GA microparticles are shown in Fig. 2a. The main differences between the silk fibroin (Fig. 2a, light green line) and the arabic gum (Fig. 2a, purple line) profiles resides in the presence of the Amide II peak and in the absence of the characteristic carbohydrate region between 1200 cm$^{-1}$ and 800 cm$^{-1}$. The spectra of GA nc (non-crosslinked) and GA c (crosslinked) microparticles (Fig. 2a, blue and black lines, respectively) include both these regions and show a broad band at around 3600 ~ 3000 cm$^{-1}$, indicating enhanced hydrogen bonding. This implied that hydrogen bonding is involved in the interaction between SF and GA. The Amide I peaks of GA nc and GA c microparticles were identified with significant shifting from the SF Amide I peak. A possible explanation for this shifting can be related to the particle formation process and the strong electrostatic interactions between SF and GA. The same mechanism could explain the shifting of the Amide II from 1512 cm$^{-1}$, in the case of pure SF, to 1541 cm$^{-1}$ and 1533 cm$^{-1}$ in the spectra of GA nc and GA c, respectively. Moreover, a significant shifting of Amide I and II peaks at lower wavenumbers and the appearance of a more pronounced shoulder at 1260 cm$^{-1}$ in the GA c spectrum suggest the silk fibroin chains transition to a β-sheet conformation, as reported in the literature. In particular, the appearance of the 1629 cm$^{-1}$ peak in the crosslinked sample was observed.

With the encapsulation of the lysozyme in the particles, the peaks of the resulting GA-LZ nc and GA-LZ c FTIR spectra (Fig. 2a, bright green and red lines, respectively) become slightly more challenging to distinguish and identify due to similar absorbance profiles between silk fibroin and lysozyme. Except for the broader peaks in 3600 ~ 3000 cm$^{-1}$

region, which could also be due to the humidity and water vapour content in the samples or in the pumping system during the WVA treatment, the GA-LZ nc and GA-LZ c spectra seem to overlap quite perfectly (e.g. Amide I peak located at 1659 $cm^{-1}$). Looking closer (Fig. 2b), a small shoulder appears in the GA-LZ c spectrum at 1628 $cm^{-1}$which suggests that a higher number of β-sheet domains has been formed with the post-fabrication treatment.

In the spectra of the GX nc and GX c samples (Fig. 2c, blue and black lines, respectively), we can easily assign every peak to bond vibrations of either silk fibroin or Xanthan gum. The main differences between the SF protein sample and the Xanthan gum sample are the presence of the Amide II peak and the absence of the characteristic carbohydrate region between 1200 $cm^{-1}$ and 800 $cm^{-1}$. The spectra of GX nc and GX c samples include both these regions and show a broad band at around 3600 ~ 3000 $cm^{-1}$, indicating enhanced hydrogen bonding. This implied that hydrogen bonding is involved in the interaction between SF and GX. The Amide I peaks of GX nc (1659 $cm^{-1}$) and GX c (1659 $cm^{-1}$ and 1630 $cm^{-1}$) samples were identified with significant shifting from the SF Amide I peak (1628 $cm^{-1}$). The possible explanation for this shifting can be related to the particle formation process and the strong electrostatic interactions between SF and GX. The same mechanism could explain the shifting of the Amide II from 1512 $cm^{-1}$ in the case of pure SF to 1540 $cm^{-1}$ and 1532 $cm^{-1}$ in the spectra of GX nc and GX c samples, respectively. Unlike what observed for Arabic gum sample, the Xanthan gum spectrum shows an absorption peak at 1732 $cm^{-1}$, indicating the presence of C = O stretching of carbonyl ester; this peak can be also identified in the spectra of the GX nc and GX c samples. If we compare the GX nc and GX c samples, a significant shifting of the Amide II peak at lower wavenumbers and the appearance of the Amide I peak at 1630 $cm^{-1}$ was observed, which indicates the presence of β-sheet-rich proteins. Indeed, the maxima absorption for α-helix, β-sheet and random coil structures are at 1655 $cm^{-1}$, 1630 $cm^{-1}$ and 1645 $cm^{-1}$, respectively, and they are all included in the frequency range of the Amide I band. As for the GX c sample, a small shoulder is visible at 1269 $cm^{-1}$, which confirms the silk fibroin chains transition to a β-sheet conformation, as reported in the literature (Fang et al., 2015).

With the encapsulation of the lysozyme in the particles, the peaks of the resulting GX-LZ nc and GX-LZ c FTIR spectra (Fig. 2c, bright green and red lines, respectively) are difficult to accurately recognize and distinguish due to the similar absorbance profiles between SF and the lysozyme, as already mentioned for the GA-LZ samples. As previously discussed for the samples with the Arabic gum and lysozyme, the GX-LZ nc and GX-LZ c spectra may seem very similar. The main difference is referred to the Amide I (i.e. the Amide I band at 1659 $cm^{-1}$ is split into two components at 1657 $cm^{-1}$ and 1630 $cm^{-1}$) and Amide II peaks (shifting from 1539 $cm^{-1}$ to 1533 $cm^{-1}$), as shown in Fig. 2d. Looking closer (Fig. 2d), a small shoulder is visible in the GX-LZ c spectrum also at 1700 $cm^{-1}$. All these data confirm that a higher number of β-sheet domains have been formed with the post-fabrication treatment.

The microparticles internal structure and its evolution upon cross-linking has been observed by SAXS experiments on the samples fully hydrated in water. Fig. 2 (e,f) reports the scattered intensity profiles of GA and GX microparticles (in the q range 0.07 nm-1 < q < 6 $nm^{-1}$), before and after the cross-linking treatment, together with the ones of their pristine components (silk fibroin, Arabic gum, Xanthan gum) in the high-q range (0.7 $nm^{-1}$ < q < 6 $nm^{-1}$). The intensity profile of fibroin corresponds to the local arrangement of fibroin molecules, with a radius of gyration of about 8 nm (Martel et al., 2008). The intensity spectra of gums display characteristic features of interacting colloids and polysaccharide chains, with the presence of a structure factor peak, in agreement with the literature (Atgié et al., 2019; Villetti et al., 2000). The q-position of the structure peaks, qpeak = 0.36 $nm^{-1}$ for Arabic gum and qpeak = 0.7 $nm^{-1}$ for Xanthan gum, are related to the characteristic internal distance d = 2π/qpeak between interacting chains, 17.2 nm for Arabic gum and 9.2 nm for Xanthan gum.

The spectra of GA and GX microparticles before cross-linking, maintain a behaviour quite similar to those of pristine gums in the high-q region, corresponding to the local arrangement of chains. Interestingly, in GA the structure peak is still identifiable in the same position (qpeak = 0.36 $nm^{-1}$), while in GX the structure peak becomes less pronounced and shifts to higher q values as for closer, less repulsive chains. In the low-q region, giving information on the internal structure of microparticles on the tens of nms length scale, the intensity decays of GA (nc) and GX (nc) are proportional to $q^{-2.7}$ and $q^{-3}$ respectively, characteristic for mass fractals, as expected for a polymeric matrix (Lidner and Zemb, 2002).

Intensity spectra of GA and GX microparticles after cross-linking are reported in Fig. 2 e, f (red symbols). The cross-linking treatment affects the internal arrangement of microparticles mainly in the intermediate q region, corresponding to the nms length scale. In the GA c system, the structure peak at qpeak = 0.36 $nm^{-1}$ moves to qpeak = 0.25 $nm^{-1}$, corresponding to a larger characteristic distance of 24 nm within the polymeric matrix. In the GX c sample the intensity contribution of fibroin in the 0.1 $nm^{-1}$ < q < 0.5 $nm^{-1}$ region disappears, suggesting a change in the conformation of fibroin. The encapsulation of lysozyme does not affect the main features of the intensity spectra (Fig. 2 g, h) revealing a similar internal structure of GA-LZ c and GX-LZ c microparticles in the presence of the lysozyme. In the GA-LZ c system, a slight looser arrangement of the polymeric matrix is observed on the tens of nm length scale, with the vanishing of the structure peak.

Overall, the results reveal an intimate entanglement of fibroin with gums, affecting the local arrangement of polymers within the matrix up to the nm length scale and reducing electrostatic repulsion between chains. The interaction is more effective after cross-linking treatment and probably facilitated by a conformational change of fibroin.

### 3.2. Hydration properties and degradation

Hydration behaviour is crucial to guarantee a balance between the exudate absorption and the wound bed dehydration, both essential features in the granulation phase (Ruggeri et al., 2020; Saporito et al, 2018). Fig. 3 reports the hydration properties as swelling index (top left panel) and weight residues (%) of the microparticles (top right panel) after 24 and 48 h of incubation in SAS. GX-based microparticles show a higher swelling index and weight loss than GA-based microparticles, suggesting a faster degradation. Moreover, the lysozyme loading does not seem to alter the microparticles swelling and degradation behaviour. After 48 h, SEM images show that the microparticles become rougher and partially fused to form conglomerates. The microparticles are characterized by a high hydrophilicity and the aqueous medium causes the formation of bridge in the contact points among particles. In detail, the greater swelling and degradation of GX-based microparticles could be related to the different structure of the polymer: GX, having a higher molecular weight than GA, could interfere during the fibroin cross-linking process due to the steric hindrance, leading to the formation of a less resistant 3D structure. Despite this, the structures remain present, and this is a favourable property to enhance the interaction between the systems and the wound bed. The hydrophilicity of the scaffold should enhance cell-scaffold interaction promoting the healing process.

### 3.3. Mucoadhesion properties

Fig. 4 shows the results of the mucoadhesion measurements, expressed as maximum force of detachment, Fmax (left panel) and work of adhesion AUC (right panel) values in presence or in absence of mucin.

The results suggest that all the microparticles are characterized by good mucoadhesive properties (Fmax and AUC in presence of mucin higher than without mucin). Microparticles prove to interact with mucin glycoproteins chains, and this should prolong the residence in the periodontal pocket. In detail, the lysozyme loading seems to increase the mucoadhesive performance. This seems related to the LZ ability to strongly bind to mucin (Filatova et al., 2022; Lu et al., 2005). In

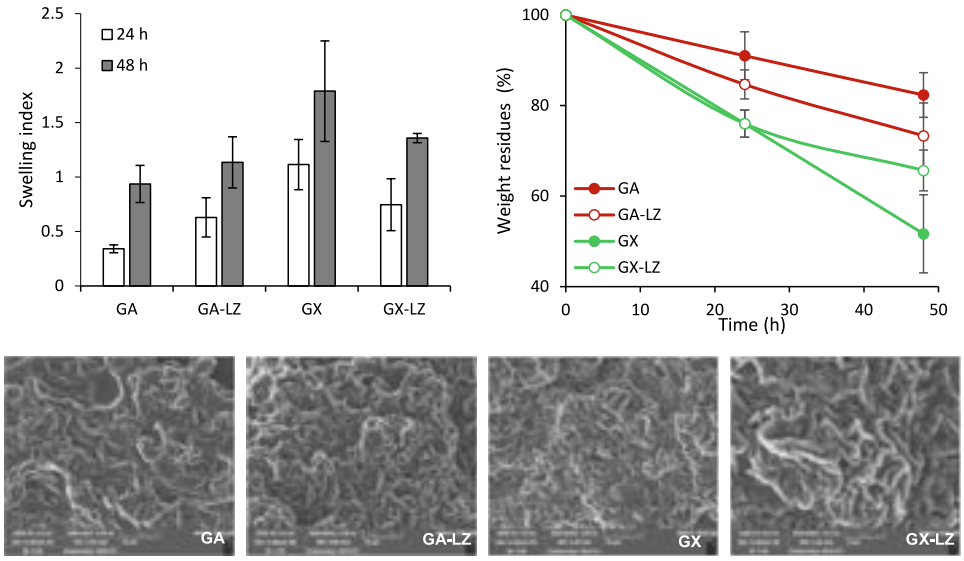


**Fig. 3.** Hydration properties of spray-dried microparticles expressed as swelling index (top left panel), weight residues (%) of microparticles after 24 and 48 h of incubation in SAS (top right panel), and SEM images of spray-dried microparticles after 48 h of incubation in SFS at 37 °C (bottom panel).

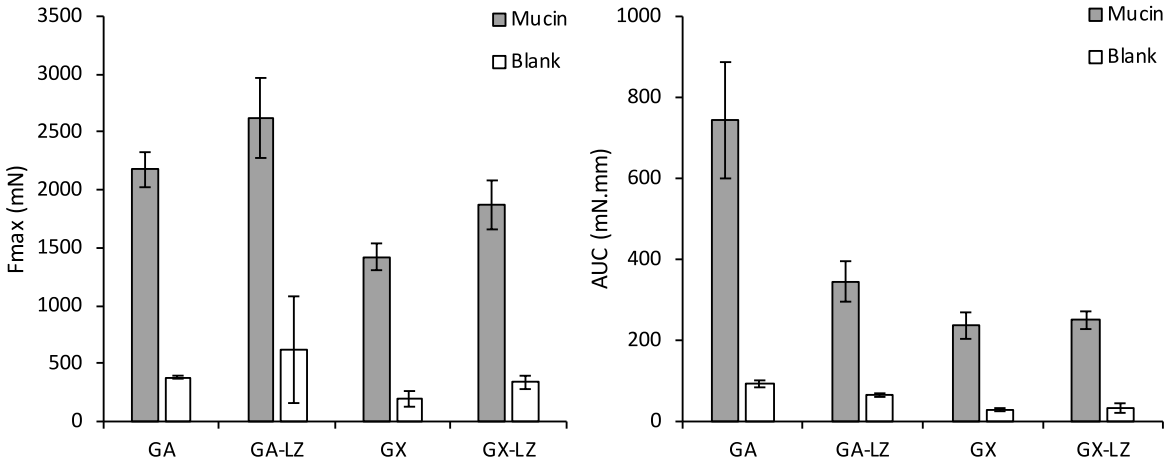


**Fig. 4.** Maximum force of detachment (left panel) and work of adhesion (right panel) values calculated for all the microparticles in presence or in absence (blank) of submaxillary bovine mucin dispersion (mean values ± sd; n = 5). ANOVA one-way; Scheffe's test ($p \leq 0.05$): a) GA Fmax mucin vs. GA Fmax blank, GA-LZ Fmax mucin vs. GA-LZ Fmax blank, GX Fmax mucin vs. GX Fmax blank, GX-LZ Fmax mucin vs. GX-LZ Fmax blank; GA-LZ Fmax mucin vs. GX Fmax mucin; b) GA AUC mucin vs. GA AUC blank, GA-LZ AUC mucin vs. GA-LZ AUC blank, GX AUC mucin vs. GX AUC blank, GX-LZ AUC mucin vs. GX-LZ AUC blank; GA AUC mucin vs. GA-LZ, GX, GX-LZ AUC mucin.

particular, it has been proved that LZ possesses a higher propensity to interact with mucin at pH 6–7 and that complexes between biomolecules occur due to electrostatic interactions between the positively charged amino groups of LZ and the negatively charged carboxyl groups of the carbohydrate shell of mucin mainly formed of sialic acid. Moreover, Van der Waals forces and hydrogen bonds are involved. Both GA and GX are reported in literature as mucoadhesive polymers: they possess an anionic character (Malik et al., 2020; Sakloetsakun et al., 2016) but the mucoadhesive behaviour is mainly related to the high number of hydroxyl groups able to form hydrogen bonds with mucin. Despite this, GA shows superior mucoadhesive potential: this could be related to the less branched structure (lower viscosity) and the consequent higher interdiffusion and interpenetration between mucin and polymer chains that strengthen the mucoadhesive interface.

The mucoadhesion in periodontal disease treatment offers several notable advantages over currently available ones, including a good retention within the periodontal pocket. Moreover, the mucoadhesion enables a local release of the loaded drugs, thus improving the efficacy and the patient's compliance (Bruschi et al., 2007; Rohani Shirvan et al., 2021; Sandri et al., 2020).

### 3.4. Lysozyme release and antibacterial properties

Lysozyme (14–15 kDa) is physiologically found in body fluids, including saliva. Salivary lysozyme is produced by the salivary glands and by neutrophil granulocytes entering the mouth and it is also present in the gingival crevicular fluid. The encapsulation efficiency was calculated to be 94.73 and 95.12% for GA-LZ and GX-LZ microparticles, respectively. This result could be due to the high lysozyme solubility in the aqueous polymer solution, that guarantees a homogenous blending. The release profile of lysozyme from the microparticles is shown in Fig. 5 (top panel).

The release profiles comprise two steps: an initial step where a steep increase of LZ released is present within the first 24 h, independently of the composition (burst release), and a second stage where a sustained release is evident up to 7 days (168 h).

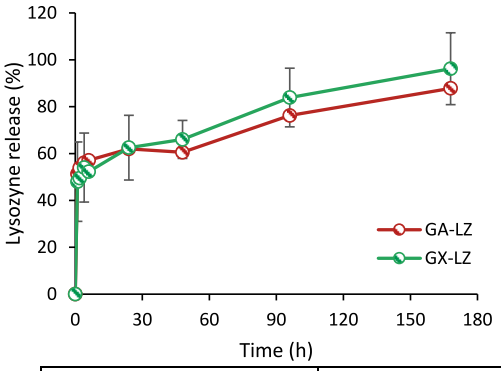


| Time (h) | GA-LZ (UI/ml) | GX-LZ (UI/ml) |
|---|---|---|
| 1 | 5460±763 | 5244±1850 |
| 2 | 5726±498 | 5404±200 |
| 4 | 5948±404 | 5884±1627 |
| 6 | 6046±302 | 4968±1217 |
| 24 | 6553±440 | 6791±1456 |
| 48 | 6384±538 | 6755±1010 |
| 96 | 8046±1275 | 8231±1797 |
| 168 | 9264±447 | 10426±1817 |

| *Streptococcus mutans* | GA-LZ | GX-LZ | Ampicillin |
|---|---|---|---|
| MIC | 450 | 219 | 0.25 |
| MBC | 792 | 469 | 0.5 |

**Fig. 5.** Cumulative percentage release of Lysozyme from the microparticles (top left panel) at predetermined times and activity of the released lysozyme (UI/ml) (top right panel) (mean value ± s.d.; n = 3); MIC and MBC values for the microparticles (GA-LZ and GX-LZ) against *Streptococcus mutans* ATCC 25175 compared to ampicillin.

The two behaviours are attributable to the hydration, swelling and degradation of the microparticles. In particular, the burst release is related to the partial hydration and a partial loss of integrity of the microparticles as shown with the SEM images. This phenomenon could cause a disentanglement of the polymer matrix and a fast release of the lysozyme loaded in the outer layers. The second step of the profile is mostly related to the slower hydration of the microparticles inner part and the consequent diffusion of the lysozyme across the polymeric network.

The gingival crevicular fluid in the periodontal pocket is strictly related to the inflammation. In healthy pocket is about 43 µl/day, and the flow rate is low and is about 0.03 µl/min. When a periodontitis occurs the volume and fluid flow rate dramatically increase and are about 480 µl/day and about 0.33 µl/min, respectively. Since the turnover rate of gingival fluid is 40 times/h the mucoadhesive microparticles here developed should promote the permanence of the active components, both biopolymers having wound healing properties and lysozyme possessing antimicrobial activity (Medlicott et al., 1994).

The antibacterial activity of lysozyme is manly related to its muramidase activity via hydrolysis of the β-1,4-glycosidic bonds between N-acetylmuramic acid and N-acetyl-D-glucosamine of peptidoglycan in bacterial cell wall. It is particularly effective against Gram-positive bacteria and reduced susceptibility of most Gram-negative species having peptidoglycans shielded by an outer membrane. However, in the Gram-negative bacteria lysozyme may cause membrane leakage of the outer membrane to allow reaching the peptidoglycan layer (Ferraboschi et al., 2021).

Considering these, the antimicrobial properties of the formulations have been characterized against a common microbial strain, *Streptococcus mutans,* a Gram-positive bacterium recognized as capable to form biofilms on tooth surfaces causing dental plaque and widely present in the oral cavity and in the periodontal region. Fig. 5 (bottom panel) reports MIC/MBC values of the microparticles against *S. mutans* ATCC 25175. Independently of the polymer type (GA or GX), microparticles possess MIC/MBC values extremely lower than the lysozyme concentration released, suggesting that the lysozyme concentration reached into the periodontal pocket should be always higher than MIC/MBC. Therefore, independently of the microparticles composition and considering the small volume in the pocket, the lysozyme release should determine high LZ concentration greater than 5000 UI/ml, which is higher than the MIC/MBC values against *S. mutans* and reported in literature for some bacterial strains resident in the oral cavity (Charernsriwilaiwat et al., 2012; Ferraboschi et al., 2021). Moreover, microparticles could be administered in variable amount depending on the periodontitis severity and the pocket volume.

### 3.5. *In vitro cell adhesion and proliferation*

The biocompatibility and proliferation have been evaluated towards two cell types, NHDF (normal human dermal fibroblasts) and hASCs (human adipose tissue-derived stem cells). The cell types to evaluate *in vitro* safety and effectiveness were selected considering both the model standardization and in vivo application of the systems. In particular normal human dermal fibroblasts have been selected since their proliferation and migration are deeply influenced by the evironment and the culture model is well-established and standardized (Weinreb and Nemcovsky, 2015). Parallely, human adipose stem cells, derived from adipose tissues, have been considered since they are widely used in regenerative medicine and there are evidence in literature that transplanting hASC in periodontal tissue defects regenerate dentin and cementum and organizes periodontal ligament fibers, alveolar bone structure and periodontal vessel regeneration (Tobita et al., 2008).

Fig. 6 reports fibroblasts and hASCs proliferation (left panel) and the CLSM micrographs (right panel).

Independently of the composition, microparticles are characterized by good biocompatibility towards both fibroblasts and hASCs. Moreover, the microparticles prove to sustain cell proliferation up to 6 days and in particular GX-based microparticles loaded with lysozyme significantly affects hASCs proliferation.

The CLSM analysis confirms that both fibroblasts and hASCs adhere, and spread, maintaining their native structure of the cytoskeletons characterized by fusiform and polygonal shapes, respectively.

These results suggest that the systems are conceivably scaffolds able to to sustain cell growth. The relevant fibroblasts and hASC growth in presence of both systems also loaded with LZ not only evidence the *in vitro* safety but also the systems suitability to be coadministrered in presence of hASC in vivo. Althought the microparticulate systems are designed and developed to be implanted as acellular systems, the results obtained pave the way for their employment as advance therapy medicinal products in association with hASC that are widely used in periodontal tissue engineering since demonstrate the capability to promote the regeneration of all the different specialized tissue.

### 3.6. *Preliminary preclinical evaluation on in vivo model*

The preclinical evaluation was performed in vivo in a murine model using subcutaneous implants as proof of concept to evaluate the system safety and their potential application to promote wound healing of the soft tissue loss in mild periodontitis. This model is currently used to explore the inflammatory response of the dental biomaterials in an early stage of translational research since it is well-developed and

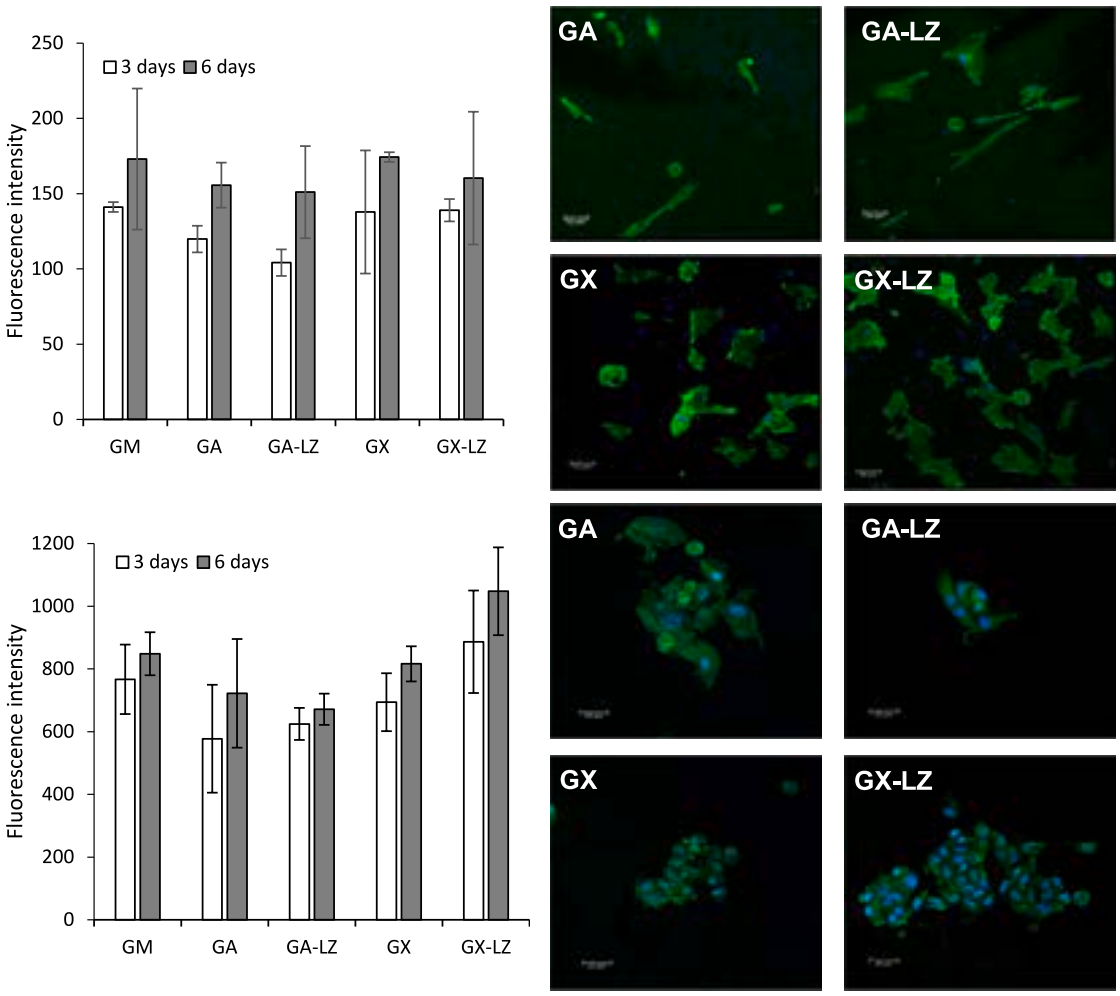


**Fig. 6.** Viability (fluorescence intensity) of fibroblasts (top left panel) or hASCs (bottom left panel) after 3 days and 6 days in contact with microparticles (GA, GA-LZ, GX, GX-LZ) in comparison to the positive control GM (growth medium, as standard growth conditions) (mean values ± s.d.; n = 5). 1-way ANOVA, Sheffé test ($p < 0.05$): Fibroblasts proliferation 3 days: GM vs. GA-LZ, GA-LZ vs. GX and GX-LZ; hASCs proliferation 3 days: GA vs. GX-LZ; hASCs proliferation 6 days: GA and GA-LZ vs. GX-LZ. Confocal laser scanning microscopy (CLSM) micrographs of fibroblasts (top right panel) or hASCs (bottom right panel) grown for 6 days onto microparticles (in blue: nuclei; in green: cytoskeleton). Scale bar: 20 μm. (For interpretation of the references to colour in this figure legend, the reader is referred to the web version of this article.)

standardized and does not cause much discomfort for animals (Wang et al., 2020). Although the lesions in the oral cavity heal faster compared to the skin, the cutaneous and gingival tissues have similar macroscopic healing patterns, including hemostasis, inflammation, proliferation, and remodeling phases. The histology of the tissues in correspondence of the implant sites is reported in Fig. 7. The tissue in correspondance with the control lesion (treated with saline solution) (Fig. 7 b) is not completely regenerated and shows several blood vessels and a residual area of granulation tissue, and PSR staining shows a small amount of still immature and not remodeled collagen in the appropriate orientation. Microparticles residues are not evident at the site of the implants and little differences are evident from the adjacent control skin. Moreover, the surface of each incisional lesion is covered with new epithelium and no signs of either fibrosis (collagen distributed in bundles) or inflammation are evident, without accumulation of macrophages, lymphocytes, or granulocytes (Ruggeri et al., 2022b).

The skin is completely regenerated after the surgical procedures, and hair follicles and sebaceous glands are almost completely restored in all the tissues where microparticles have been implanted. In particular, the epidermidis is fully restored in multiple cell layers with a fair degree of keratinization, and collagen is deposited and remodelled in an appropriate manner. Skin appendages (hair follicles and glands) are identical in number and disposition with respect to those of intact skin, and only in a very small central area of the wound is not yet completely reformed. PRS shows a continuous collagen layer, rich in orange-to-red fibers, with a pattern similar to that of the intact skin. These suggest that the microparticles do not promote neither a proinflammatory response nor the foreign body reaction.

## 4. Conclusions

Spray-drying was successfully used to prepare microparticles for the soft tissue restoration after a periodontal lesion. The developed process allowed to obtain microparticles based on gums and fibroin and loaded with lysozyme due to its antibacterial properties. Arabic and xanthan gum affected the microparticles morphology, characterized by concavities and spherical shape, respectively. Water vapor annealing was used as crosslinking process, leading to the transition from the amorphous state silk I to the crystalline silk II, thus allowing to obtain substrates insoluble in aqueous environment. The physico-chemical analysis proves that a higher number of β-sheet domains is formed after crosslinking and an intimate interaction between fibroin and gums occurred, affecting the local arrangement of the macromolecular chains. The systems were characterized by suitable swelling, degradation and mucoadhesive properties, leading to a prolonged retention in situ and a sustained release of lysozyme that reaches antimicrobial concentrations.

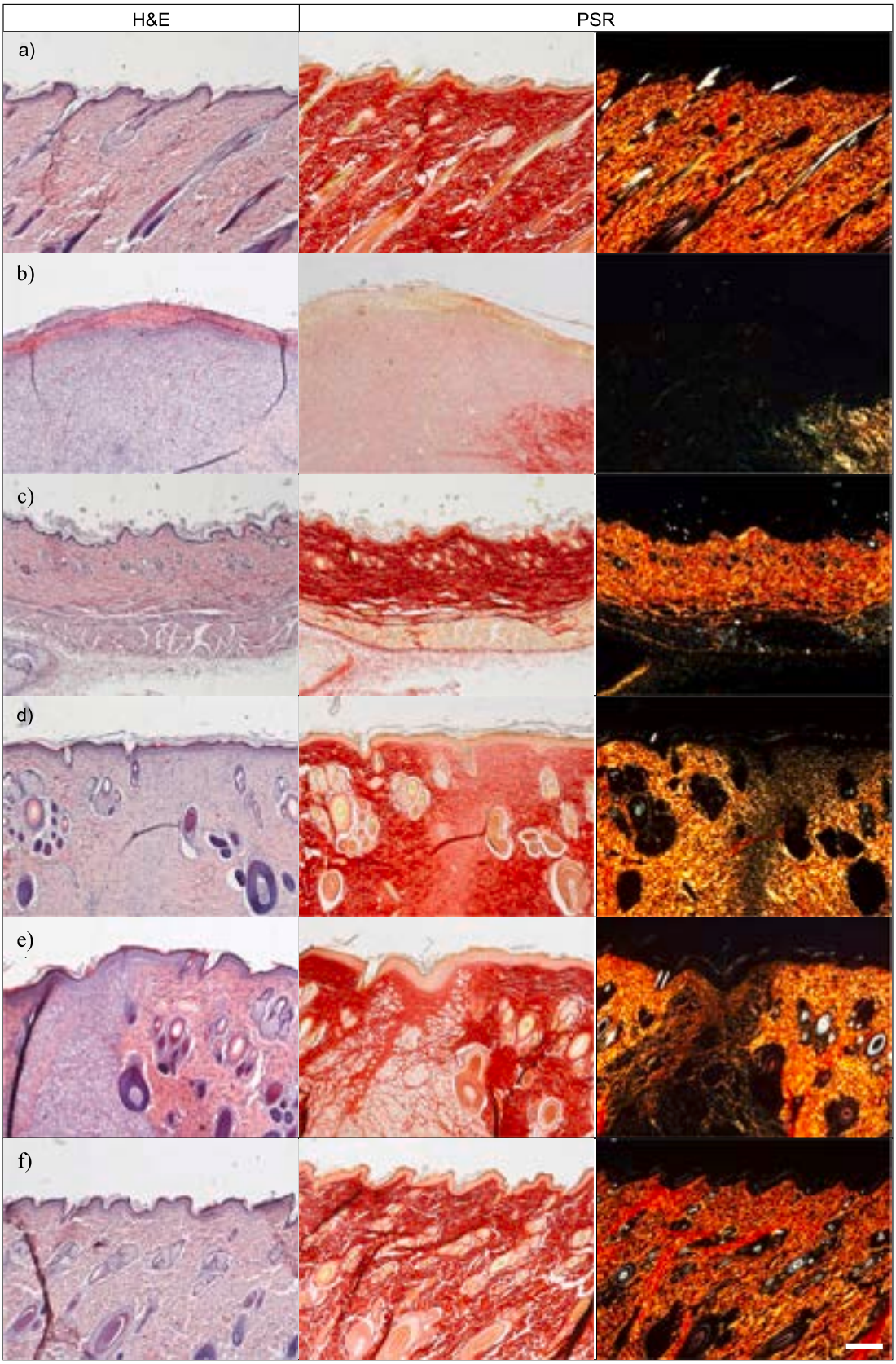


**Fig. 7.** H&E (left panel) and PSR (central panel - with bright-field images; right panel - with polarized light) sections of a) intact skin, b) lesion treated with saline solution as negative control, c) lesions treated with GA microparticles, d) lesions treated with GA-LZ microparticles, e) lesions treated with GX microparticles, f) lesions treated with GX-LZ microparticles. Scale bar: 100 μm.

In particular, GX-based microparticles offers more adaptability in terms of swelling, degradation and hydration, and proves to be effective against a common microbial strain resident in the oral cavity, *S. mutans*, simultaneoulsy promoting cell proliferation. The *in vitro* study outcomes and the encouraging preclinical results highlighted that the fibroin/xanthan gum-based microparticles could provide a biocompatible platform able to prevent periodontitis progression and to promote the healing of soft tissues in mild periodontitis.

## CRediT authorship contribution statement

**Marco Ruggeri:** Conceptualization, Data curation, Formal analysis, Investigation, Methodology, Supervision, Writing – original draft, Writing – review & editing. **Martina Lenzuni:** Data curation, Investigation. **Giulia Suarato:** Data curation, Investigation, Writing – review & editing. **Barbara Vigani:** Visualization, Data curation. **Cinzia Boselli:** Data curation, Investigation. **Antonia Icaro Cornaglia:** Data curation, Investigation. **Daniele Colombo:** Investigation. **Pietro Grisoli:** Investigation. **Caterina Ricci:** Investigation. **Elena Del Favero:** Data curation, Investigation, Formal analysis, Resources. **Silvia Rossi:** Visualization, Resources. **Athanassia Athanassiou:** Resources, Writing – review & editing. **Giuseppina Sandri:** Conceptualization, Project administration, Resources, Supervision, Writing – original draft, Writing – review & editing.

## Declaration of Competing Interest

The authors declare that they have no known competing financial interests or personal relationships that could have appeared to influence the work reported in this paper.

## Data availability

Data will be made available on request.

*Acknowledgements*

Authors thank Horizon 2020 Research and Innovation Programme under Grant Agreement No. 814607 for funding the research project, ESRF for financial support and beamtime (DOI: 10.15151/ESRF-ES-585935736) and ID02 staff for technical support, and the animal facility "Centro di servizio per la gestione unificata delle attività di stabulazione e di radiobiologia" of the University of Pavia (Italy) to host the animals and the OPBA of the University of Pavia for support in animal protocol drawing up.

This work benefited from the use of the SasView application, originally developed under NSF Award DMR-0520547. SasView also contains code developed with funding from the EC Horizon 2020 program under the SINE2020 project grant No 654000.

## References

Abrahamian, L., Pascual-LaRocca, A., Barallat, L., Valles, C., Herrera, D., Sanz, M., Nart, J., Figuero, E., 2022. Intra- and inter-examiner reliability in classifying periodontitis according to the 2018 classification of periodontal diseases. J. Clin. Periodontol. 49, 732–739. https://doi.org/10.1111/jcpe.13618.

Abusleme, L., Hoare, A., Hong, B.Y., Diaz, P.I., 2021. Microbial signatures of health, gingivitis, and periodontitis. Periodontol 2000 (86), 57–78. https://doi.org/10.1111/prd.12362.

Albandar, J.M., Susin, C., Hughes, F.J., 2018. Manifestations of systemic diseases and conditions that affect the periodontal attachment apparatus: Case definitions and diagnostic considerations. J. Clin. Periodontol. 45 https://doi.org/10.1002/JPER.16-0480. S171–S189.

Atgié, M., Garrigues, J.C., Chennevière, A., Masbernat, O., Roger, K., 2019. Gum Arabic in solution: Composition and multi-scale structures. Food Hydrocoll. 91, 319–330. https://doi.org/10.1016/j.foodhyd.2019.01.033.

Bilal, M., Munir, H., Khan, M.I., Khurshid, M., Rasheed, T., Rizwan, K., Franco, M., Iqbal, H.M.N., 2022. Gums-based engineered bio-nanostructures for greening the 21st-century biotechnological settings. Crit. Rev. Food Sci. Nutr. 62, 3913–3929. https://doi.org/10.1080/10408398.2020.1871318.

Bruschi, M.L., Jones, D.S., Panzeri, H., Gremião, M.P., de Freitas, O., Lara, E.H., 2007. Semisolid systems containing propolis for the treatment of periodontal disease: in vitro release kinetics, syringeability, rheological, textural, and mucoadhesive properties. J. Pharm. Sci. 96, 2074–2089. https://doi.org/10.1002/jps.20843.

Budai-Szűcs, M., Ruggeri, M., Faccendini, A., Léber, A., Rossi, S., Varga, G., Bonferoni, M. C., Vályi, P., Burián, K., Csányi, E., Sandri, G., Ferrari, F., 2021. Electrospun Scaffolds in Periodontal Wound Healing. Polymers (Basel) 13, 307. https://doi.org/10.3390/polym13020307.

Carrizales-Sepúlveda, E.F., Ordaz-Farías, A., Vera-Pineda, R., Flores-Ramírez, R., 2018. Periodontal Disease, Systemic Inflammation and the Risk of Cardiovascular Disease. Heart Lung Circ. 27, 1327–1334. https://doi.org/10.1016/j.hlc.2018.05.102.

Charernsriwilaiwat, N., Opanasopit, P., Rojanarata, T., Ngawhirunpat, T., 2012. Lysozyme-loaded, electrospun chitosan-based nanofiber mats for wound healing. Int. J. Pharm. 427, 379–384. https://doi.org/10.1016/j.ijpharm.2012.02.010.

Dabestani, M., Yeganehzad, S., 2019. Effect of Persian gum and Xanthan gum on foaming properties and stability of pasteurized fresh egg white foam, Food Hydrocolloids, 87, 550–560. http://doi.org/10.1016/j.foodhyd.2018.08.030.

Dekina, S., Romanovska, I., Ovsepyan, A., Tkach, V., Muratov, E., 2016. Gelatin/carboxymethyl cellulose mucoadhesive films with lysozyme: Development and characterization. Carbohydr. Polym. 20, 208–215. https://doi.org/10.1016/j.carbpol.2016.04.006.

Dubey, P., Murab, S., Karmakar, S., Chowdhury, P.K., Ghosh, S., 2015. Modulation of Self-Assembly Process of Fibroin: An Insight for Regulating the Conformation of Silk Biomaterials. Biomacromolecules 16, 3936–3944. https://doi.org/10.1021/acs.biomac.5b01258.

Fang, G., Zheng, Z., Yao, J., Chen, M., Tang, Y., Zhong, J., Qi, Z., Li, Z., Shao, Z., Chen, X., 2015. Tough protein-carbon nanotube hybrid fibers comparable to natural spider silks. J. Mater. Chem. B 3, 3940–3947. https://doi.org/10.1039/C5TB00448A.

Faria, S., Petkowicz, C.L., Morais, S.A.L., Terrones, M., Resende, M.M., França, F., Cardoso, V.L., 2011. Characterization of xanthan gum produced from sugar cane broth. Carbohydr. Polym. 86, 469–476. https://doi.org/10.1016/j.carbpol.2011.04.063.

Ferraboschi, P., Ciceri, S., Grisenti, P., 2021. Applications of Lysozyme, an Innate Immune Defense Factor, as an Alternative Antibiotic. Antibiotics 10, 1534. https://doi.org/10.3390/antibiotics10121534.

Filatova, L., Emelianov, G., Balabushevich, N., Klyachko, N., 2022. Supramolecular assemblies of mucin and lysozyme: Formation and physicochemical characterization. Process Biochem. 113, 97–106. https://doi.org/10.1016/j.procbio.2021.12.022.

Gavini, E., Rassu, G., Muzzarelli, C., Cossu, M., Giunchedi, P., 2008. Spray-dried microspheres based on methylpyrrolidinone chitosan as new carrier for nasal administration of metoclopramide. Eur. J. Pharm. Biopharm. 68, 245–252. https://doi.org/10.1016/j.ejpb.2007.05.002.

Graetz, C., Mann, L., Krois, J., Sälzer, S., Kahl, M., Springer, C., Schwendicke, F., 2019. Comparison of periodontitis patients' classification in the 2018 versus 1999 classification. J. Clin. Periodontol. 46, 908–917. https://doi.org/10.1111/jcpe.13157.

Griffen, A.L., Beall, C.J., Campbell, J.H., Firestone, N.D., Kumar, P.S., Yang, Z.K., Podar, M., Leys, E.J., 2012. Distinct and complex bacterial profiles in human periodontitis and health revealed by 16S pyrosequencing. ISME J. 6, 1176–1185. https://doi.org/10.1038/ismej.2011.191.

Grohe, B., Mittler, S., 2021. Advanced non-fluoride approaches to dental enamel remineralization: The next level in enamel repair management. Biomater Biosyst. 4, 100029. https://doi.org/10.1016/j.bbiosy.2021.100029.

Guzman-Puyol, S., Heredia-Guerrero, J.A., Ceseracciu, L., Hajiali, H., Canale, C., Scarpellini, A., Cingolani, R., Bayer, I.S., Athanassiou, A., Mele, E., 2016. Low-cost and effective fabrication of biocompatible nanofibers from silk and Cellulose-rich materials. ACS Biomater Sci. Eng. 2, 526–534. https://doi.org/10.1021/acsbiomaterials.5b00500.

Ito, T., Komiya-Ito, A., Arataki, T., Furuya, Y., Yajima, Y., Yamada, S., Okuda, K., Kato, T., 2008. Relationship between antimicrobial protein levels in whole saliva and periodontitis. J. Periodontol. 79, 316–322. https://doi.org/10.1902/jop.2008.070348.

Johari, N., Moroni, L., Samadikuchaksaraei, A., 2020. Tuning the conformation and mechanical properties of silk fibroin hydrogels. Eur. Polym. J. 134, 109842. https://doi.org/10.1016/j.eurpolymj.2020.109842.

Kim, J.H., Park, C.H., Perez, R.A., Lee, H.Y., Jang, J.H., Lee, H.H., Wall, I.B., Shi, S., Kim, H.W., 2014. Advanced biomatrix designs for regenerative therapy of periodontal tissues. J. Dent. Res. 93, 1203–1211. https://doi.org/10.1177/0022034514540682.

Könönen, E., Gursoy, M., Gursoy, U.K., 2019. Periodontitis: A Multifaceted Disease of Tooth-Supporting Tissues. J. Clin. Med. 8, 1135. https://doi.org/10.3390/jcm8081135.

Kumar, A., Rao, K.M., Han, S.S., 2018. Application of xanthan gum as polysaccharide in tissue engineering: A review. Carbohydr. Polym. 15, 128–144. https://doi.org/10.1016/j.carbpol.2017.10.009.

Lidner, P., Zemb, T., 2002. Eds. Neutrons, x-rays and light: scattering methods applied to soft condensed matter, Amsterdam, North-Holland.

Lu, C., Kostanski, L., Ketelson, H., Meadows, D., Pelton, R., 2005. Hydroxypropyl guar-borate interactions with tear film mucin and lysozyme. Langmuir 21, 10032–10037. https://doi.org/10.1021/la050988g.

Malik, N.S., Ahmad, M., Minhas, M.U., Tulain, R., Barkat, K., Khalid, I., Khalid, Q., 2020. Chitosan/Xanthan Gum Based Hydrogels as Potential Carrier for an Antiviral Drug: Fabrication, Characterization, and Safety Evaluation. Front. Chem. 8, 50. https://doi.org/10.3389/fchem.2020.00050.

Martel, A., Burghammer, M., Davies, R., Di Cola, E., Vendrely, C., Riekel, C., 2008. Silk fiber assembly studied by synchrotron radiation SAXS/WAXS and Raman spectroscopy. J. Am. Chem. Soc. 130, 17070. https://doi.org/10.1021/ja806654t.

Medlicott, N.J., Rathbone, M.J., Tucker, I.G., Holborow, D.W., 1994. Delivery systems for the administration of drugs to the periodontal pocket. Adv. Drug Deliv. Rev. 13, 181–203. https://doi.org/10.1016/0169-409X(94)90033-7.

Onishi, T., Umemura, S., Yanagawa, M., Matsumura, M., Sasaki, Y., Ogasawara, T., Ooshima, T., 2008. Remineralization effects of gum arabic on caries-like enamel lesions. Arch. Oral Biol. 53, 257–260. https://doi.org/10.1016/j.archoralbio.2007.10.004.

Park, C.H., 2019. Biomaterial-Based Approaches for Regeneration of Periodontal Ligament and Cementum Using 3D Platforms. Int. J. Mol. Sci. 20, 4364. https://doi.org/10.3390/ijms20184364.

Park, C.H., Kim, K.H., Lee, Y.M., Giannobile, W.V., Seol, Y.J., 2017. 3D Printed, Microgroove Pattern-Driven Generation of Oriented Ligamentous Architectures. Int. J. Mol. Sci. 18, 1927. https://doi.org/10.3390/ijms18091927.

Pietrzyńska, M., Voelkel, A., 2017. Stability of simulated body fluids such as blood plasma, artificial urine and artificial saliva. Microchem. J. 134, 197–201. https://doi.org/10.1016/j.microc.2017.06.004.

Pignatelli, A., Perotto, G., Nardini, M., Cancedda, R., Mastrogiacomo, M., Athanassiou, A., 2018. Electrospun silk fibroin fibers for storage and controlled release of human platelet lysate. Acta Biomater. 73, 365–376. https://doi.org/10.1016/j.actbio.2018.04.025.

Pritchard, E.M., Valentin, T., Panilaitis, B., Omenetto, F., Kaplan, D.L., 2013. Antibiotic-Releasing Silk Biomaterials for Infection Prevention and Treatment. Adv. Funct. Mater. 23, 854–861. https://doi.org/10.1002/adfm.201201636.

Qi, Y., Wang, H., Wei, K., Yang, Y., Zheng, R.Y., Kim, I.S., Zhang, K.Q., 2017. A Review of Structure Construction of Silk Fibroin Biomaterials from Single Structures to Multi-Level Structures. Int. J. Mol. Sci. 18, 237. https://doi.org/10.3390/ijms18030237.

Reynolds, I., Duane, B., 2018. Periodontal disease has an impact on patients' quality of life. Evid. Based Dentistry 19, 14–15. https://doi.org/10.1038/sj.ebd.6401287.

Rohani Shirvan, A., Hemmatinejad, N., Bahrami, S. H., Bashari, A., 2021. Fabrication of multifunctional mucoadhesive buccal patch for drug delivery applications. Journal of Biomedical Materials Research Part A, 109, 2640–2656. http://doi.org/10.1002/jbm.a.37257.

Ruggeri, M., Bianchi, E., Rossi, S., Vigani, B., Bonferoni, M.C., Caramella, C., Sandri, G., Ferrari, F., 2020. Nanotechnology-Based Medical Devices for the Treatment of Chronic Skin Lesions: From Research to the Clinic. Pharmaceutics 12, 815. https://doi.org/10.3390/pharmaceutics12090815.

Ruggeri, M., Bianchi, E., Rossi, S., Boselli, C., Icaro Cornaglia, A., Malavasi, L., Carzino, R., Suarato, G., Sánchez-Espejo, R., Athanassiou, A., Viseras, C., Ferrari, F., Sandri, G., 2022. Maltodextrin-amino acids electrospun scaffolds cross-linked with Maillard-type reaction for skin tissue engineering. Biomater. Adv. 133, 112593. https://doi.org/10.1016/j.msec.2021.112593.

Ruggeri, M., Vigani, B., Boselli, C., Icaro Cornaglia, A., Colombo, D., Sànchez-Espejo, R., Del Favero, E., Mandras, N., Roana, J., Cavallo, J., Cantù, L., Viseras, C., Rossi, S., Sandri, G., 2022. Smart nano-in microparticles to tackle bacterial infections in skin tissue engineering. Materials Today Bio 16, 100418. https://doi.org/10.1016/j.mtbio.2022.100418.

Sakloetsakun, D., Preechagoon, D., Bernkop-Schnürch, A., Pongjanyakul, T., 2016. Chitosan-gum Arabic polyelectrolyte complex films: physicochemical, mechanical and mucoadhesive properties. Pharm. Dev. Technol. 21, 590–599. https://doi.org/10.3109/10837450.2015.1035727.

Sandri, G., Rossi, S., Ferrari, F., Bonferoni, M.C., Zerrouk, N., Caramella, C., 2004. Mucoadhesive and penetration enhancement properties of three grades of hyaluronic acid using porcine buccal and vaginal tissue, Caco-2 cell lines, and rat jejunum. J. Pharm. Pharmacol. 56, 1083–1090. https://doi.org/10.1211/0022357044085.

Sandri, G., Ruggeri, M., Rossi, S., Bonferoni, M.C., Vigani, B., Ferrari, F., 2020. (Trans) buccal drug delivery. In: Pedro Martins, J., Santos, H.A. (Eds.), Nanotechnology for Oral Drug Delivery. Academic Press, London, pp. 225–250.

Saporito, F., Sandri, G., Rossi, S., Bonferoni, M.C., Riva, F., Malavasi, L., Caramella, C., Ferrari, F., 2018. Freeze dried chitosan acetate dressings with glycosaminoglycans and traxenamic acid. Carbohydr. Polym. 15, 408–417. https://doi.org/10.1016/j.carbpol.2017.12.066.

Scalia, A., Zaccagnini, P., Armandi, M., Latini, G., Versaci, D., Lanzio, V., Varzi, A., Passerini, S., Lamberti, A., 2021. Tragacanth Gum as Green Binder for Sustainable Water-Processable Electrochemical Capacitor. ChemSusChem 14, 356–362. https://doi.org/10.1002/cssc.202001754.

Shaddox, L.M., Walker, C.B., 2010. Treating chronic periodontitis: current status, challenges, and future directions. Clin. Cosmet. Investig. Dent. 2, 79–91.

Sheng, X., Fan, L., He, C., Zhang, K., Mo, X., Wang, H., 2013. Vitamin E-loaded silk fibroin nanofibrous mats fabricated by green process for skin care application. Int. J. Biol. Macromol. 56, 49–56. https://doi.org/10.1016/j.ijbiomac.2013.01.029.

Sowunmi, A., Orodu, O., Efeovbokhan, V., Ogundare, S., 2020. Comparative dataset on the characterization of natural polymers and nanocomposites for enhanced oil recovery. Data Brief 33, 106506. https://doi.org/10.1016/j.dib.2020.106506.

Tobita, M., Uysal, A.C., Ogawa, R., Hyakusoku, H., Mizuno, H., 2008. Periodontal tissue regeneration with adipose-derived stem cells. Tissue Eng. A 14, 945–953. https://doi.org/10.1089/ten.tea.2007.0048.

Tonetti, M.S., Greenwell, H., Kornman, K.S., 2018. Staging and grading of periodontitis: Framework and proposal of a new classification and case definition. J. Periodontol. 89 https://doi.org/10.1002/JPER.18-0006. S159–S172.

Villetti, M., Borsali, R., Diat, O., Soldi, V., Fukada, K., 2000. SAXS from Polyelectrolyte Solutions under Shear: Xanthan and Na-Hyaluronate Examples. Macromolecules 33, 9418–9422. https://doi.org/10.1021/ma000971z.

Wang, B., Wang, J., Shao, J., Kouwer, P.H.J., Bronkhorst, E.M., Jansen, J.A., Walboomers, X.F., Yang, F., 2020. A tunable and injectable local drug delivery system for personalized periodontal application. J. Control. Release 324, 134–145. https://doi.org/10.1016/j.jconrel.2020.05.004.

Weinreb, M., Nemcovsky, C.E., 2015. In vitro models for evaluation of periodontal wound healing/regeneration. Periodontol 2000 (68), 41–54. https://doi.org/10.1111/prd.12079.

Wu, T., Wu, C., Fu, S., Wang, L., Yuan, C., Chen, S., Hu, Y., 2017. Integration of lysozyme into chitosan nanoparticles for improving antibacterial activity. Carbohydr. Polym. 155, 192–200. https://doi.org/10.1016/j.carbpol.2016.08.076.

Xiao, L., Ni, W., Zhao, X., Guo, Y., Li, X., Wang, F., Luo, G., Zhan, R., Xu, X., 2021. A moisture balanced antibacterial dressing loaded with lysozyme possesses antibacterial activity and promotes wound healing. Soft Matter 17, 3162–3173. https://doi.org/10.1039/D0SM02245D.

Yang, S., Zhang, Q., Wang, J., Liu, Y., Lu, S., Li, M., Kaplan, D.L., 2013. Silk fibroin/chondroitin sulfate/hyaluronic acid ternary scaffolds for dermal tissue reconstruction. Acta Biomater. 9, 6771–6782. https://doi.org/10.1016/j.actbio.2013.02.016.

Zhang, Y., Huang, J., Huang, L., Liu, Q., Shao, H., Hu, X., Song, L., 2016. Silk Fibroin-Based Scaffolds with Controlled Delivery Order of VEGF and BDNF for Cavernous Nerve Regeneration. ACS Biomater Sci. Eng. 2, 2018–2025. https://doi.org/10.1021/acsbiomaterials.6b00436.

Zhang, S., Yu, N., Arce, R.M., 2020. Periodontal inflammation: Integrating genes and dysbiosis. Periodontol 2000 (82), 129–142. https://doi.org/10.1111/prd.12267.